



1 **Spatial and radiometric characterization of multi-spectrum**
2 **satellite images through multifractal analysis**

3
4 **Carmelo Alonso^{1,2}, Ana M. Tarquis^{2,3}, Ignacio Zúñiga⁴ and Rosa M. Benito²**

5
6 ¹Earth Observation Systems, Indra Sistemas S.A., Madrid, Spain.

7
8 ²Grupo de Sistemas Complejos, U.P.M, Madrid, Spain.

9
10 ³CEIGRAM, E.T.S.I.A.A.B., U.P.M, Madrid, Spain.

11
12 ⁴Dpt. Física Fundamental, Facultad de Ciencias, Universidad Nacional de Educación a
13 Distancia (UNED), Madrid, Spain.

14
15
16
17 Corresponding author: Ana M. Tarquis (anamaria.tarquis@upm.es)

18
19



1 **Spatial and radiometric characterization of multi-spectrum** 2 **satellite images through multifractal analysis**

3

4 **Abstract:** Several studies point out that vegetation indexes can be used to estimate root
5 zone soil moisture and earth surface images, obtained by high resolution satellites, give
6 presently huge information on these indexes based in several wavelengths data. Because of
7 the potential capacity for systematic observations at various scales, remote sensing technology
8 extends possible data archives from present time to over several decades back. For this
9 advantage, enormous efforts have been made by researchers and application specialists to
10 delineate vegetation indexes from local scale to global scale by applying remote sensing
11 imagery.

12 In this work, four bands images have been considered, involved in these vegetation indexes,
13 taken by satellites IKONOS-2 and LANDSAT-7 of the same geographic location to study the
14 effect of both spatial (pixel size) and radiometric (number of bits coding the image) resolution
15 on these wavelength bands.

16 In order to do so, a multifractal analysis of these multi-spectral images was applied in each of
17 these bands. The results showed that spatial resolution has a similar scaling effect in the four
18 bands, but radiometric resolution has a larger influence in Blue and Green bands than in Red
19 and Near InfraRed bands. This information should be taken in to account when vegetation
20 indexes based on different satellite sensors are obtained.

21

22

23 **Keywords:** vegetation index, wavelengths pattern, multifractal spectrum

24



1 **1 Introduction**

2 Soil moisture is a critical condition affecting interaction of land surface and atmosphere.
3 Remotely sensed data is an important source of information and it can indirectly measure soil
4 moisture in space and time. However, the signal only penetrates the top few centimeters, and
5 soil moisture at deeper layers must be estimated. One method to estimate soil moisture at
6 deeper layers is through vegetation indices. Several authors have investigating the potential of
7 vegetation indices to estimate root zone soil moisture. The Normalized Difference Vegetation
8 Index (NDVI) and Enhanced Vegetation Index (EVI) have been used by several authors
9 (Wang et al., 2007; Ben-Ze'ev et al., 2006; Deng et al., 2007) in different conditions finding
10 significant estimations with root zone soil moisture. For the estimation of these indexes NIR,
11 Red and Blue wavelengths are needed (Huete et al., 2014).

12

13 The images provided by the satellites show the land surface in a wide range of wavelengths
14 (from visible to thermal infrared or microwaves) and also with a great variety of spatial
15 resolutions (from a few kilometres to tens of centimeters). The analysis of these varied images
16 and their synergic possibilities are a challenging problem especially with new sensors, which
17 have small spatial resolution and a large range of radiometric quantification. Fractal analysis
18 offers significant potential for improvement in the measurement and analysis of spatially and
19 radiometrically complex remote sensing data. This analysis also provides quantitative insight
20 on the spatial complexity in the information of the landscape contained within these data.

21

22 In the general mathematical framework of fractal geometry many analytical methods have
23 been developed; to name a few: textural homogeneity has been characterized using the fractal
24 dimension (Fioravanti, 1994); it has also been used as a spatial measure for describing the
25 complexity of remote sensing imagery (Lam and De Cola, 1993); changes in the image
26 complexity have been detected through the spectral range of hyperspectral images affecting
27 the fractal dimension (Qiu et al. 1999); similarly De Cola (1989) and Lam (1990) have found
28 that fractal dimension also depends on the spectral bands of Landsat TM imagery.

29



1 Motivated by the fractal geometry of sets (Mandelbrot, 1983), the development of multifractal
2 theory, introduced in the context of turbulence, has been applied in many areas such as
3 earthquake distribution analysis (Hirata and Imoto, 1991), soil pore characterization
4 (Kravchenko et al. 1999; Tarquis et al. 2003), image analysis (Sánchez et al. 1992) or remote
5 sensing (Tessier et al., 1993; Cheng and Agterberg, 1996; Schmitt et al., 1997; Laferrière and
6 Gaonac'h, 1999; Cheng, 1999; Lovejoy et al., 2001b; Du and Yeo, 2002; Parrinello and
7 Vaughan, 2002; Harvey et al., 2002; Turiel et al. 2005).

8

9 The acquisition of remotely sensed multiple spectral images is thus a unique source of data
10 for determining the scale invariant characteristics of the radiance fields related to many
11 factors, such as soil and bedrock chemical composition, humidity content and surface
12 temperature (e.g., Laferrière and Gaonac'h, 1999; Maitre and Pinciroli, 1999; Lovejoy et al.,
13 2001a, b; Harvey et al., 2002; Beaulieu and Gaonac'h, 2002; Gaonac'h et al., 2003; Cheng,
14 2004). In the multifractal scheme used, the satellite image is considered as a singular measure
15 and it is analyzed through a multifractal (MF) spectrum, which gives either geometrical or
16 probabilistic information about the pixels distribution with the same singularity.

17

18 The aim of this work is to characterize by MF analysis the image patterns in the wavelength
19 ranges used for NDVI, EVI and Green bands. In order to investigate how the image
20 information is affected by the sampling with different spatial and radiometric resolutions, we
21 have also analyzed images of the same site but acquired by two different satellites: Landsat-7
22 and Ikonos-2.

23

24 We present a comparative analysis of multifractal (MF) tools applied to multi-spectral images
25 obtained by IKONOS-2 and LANDSAT-7. Both satellites have several bands in visible and
26 near-infrared spectral regions in common that can be used in vegetation indexes estimation.
27 However the bands have different spatial resolution, 4 m for IKONOS and 30 m for
28 LANDSAT-7, and radiometric resolution, 11 and 8 bits respectively. The bands we have
29 chosen are Red (R), Green (G), Blue (B) and Near InfraRed (NIR). For each of those bands,
30 the MF spectrum has been calculated directly from the Hölder exponents α and the
31 singularities spectrum $f(\alpha)$.



2 Materials and methods

2.1 Images

As already noted, in this work we have analysed two images of the same site acquired from different satellites, Landsat-7 and Ikonos-2. Both are multi-spectral images with several bands that cover several regions of the electromagnetic spectrum in the visible and near infrared wavelength.

Landsat-7 was put in orbit in April 1999. This satellite follows a sun-synchronous orbit at 705 km of altitude, with an equatorial crossing time of 10:00 a.m. in the descending node. It requires 98.8 min to circle the Earth, tracing a worldwide reference system (WRS) of just over 230 ground paths. During at least three decades Landsat orbits over each of these paths once every 16 days in a repetitive cycle (Mika, 1997).

The main Landsat-7 sensor for Earth observation is the Enhanced Thematic Mapper Plus (ETM+). The ETM+ operates as a whiskbroom scanner and acquires data for seven spectral bands: visible (ETM+#1, from 0.45 to 0.52 μm ; ETM+#2, from 0.53 to 0.61 μm ; ETM+#3, from 0.63 to 0.69 μm), near infrared (ETM+#4, from 0.78 to 0.9 μm), shortwave infrared (ETM+#5, from 1.55 to 1.75 μm , and ETM+#7, from 2.09 to 2.35 μm) and thermal infrared (ETM+#6, from 10.4 to 12.5 μm). The ETM+ ground sampling distance (pixel size in the images) is 30 m for the six reflective bands and 60 m for the thermal band. The ETM+ also acquires images for a panchromatic band (ETM+#8, from 0.52 to 0.9 μm) with a 15 m ground sampling distance. The radiometric resolution of the Landsat-7 data is 8 bit/pixel or 256 grey levels for the pixel digital value.

Ikonos-2 was launched in September 1999. Its panchromatic sensor, with a resolution of 0.82 m, provided the first very high resolution images of the Earth's surface from EOS. The Ikonos orbit altitude is approximately 681 km, it is inclined 98.1 degrees to the equator and it provides sun-synchronous operation. The equatorial crossing time of Ikonos is 10:30 a.m. in



1 the descending node. The orbit provides daily access to sites within 45 degrees of nadir (Dial
2 et al. 2003).

3

4 The multi-spectral sensor simultaneously collects blue (IK#1, from 0.445 to 0.516 μm), green
5 (IK#2, from 0.506 to 0.595 μm), red (IK#3, from 0.632 to 0.698 μm) and near infrared (IK#4,
6 from 0.757 to 0.853 μm) bands with 3.28 meter resolution at nadir. Both images,
7 panchromatic and multi-spectral, have a radiometric resolution of 11 bits/pixel or 2048 grey
8 levels for the pixel digital value.

9

10 The Landsat-7 multi-spectral image used in this study was acquired on August 6th 2000 at
11 10:46 a.m. and it corresponds to the scene with WRS coordinates, path and row: 201 - 32.
12 This scene is located in the central region of Spain and it covers a square surface of
13 approximately 180 km side-length, located around Madrid. Solar azimuth and elevation
14 angles for this scene are 132.44 and 58.62 degrees respectively.

15

16 The Ikonos data used in this study is a multi-spectral image acquired on August 8th 2000 at
17 11:03 a.m. It covers a square area of 11 km side located near Aranjuez, south of Madrid, in
18 the central region of Spain. Solar azimuth and elevation angles for this scene are 139.5 and
19 60.79 degrees respectively. Both images were corrected geometrically to the same
20 cartographic projection: UTM, zone 30 N by a co-registration process.

21

22 The analysis has been carried out on a subset that covers (approximately) the same area in
23 both the Landsat and the Ikonos images, corresponding to a region located north the town of
24 Aranjuez. The representative elements of the land used in the selected area are: irrigate crops,
25 pastures, heaths, unirrigated land cultivations and olive groves. The Landsat subset is a
26 rectangle of 772 x 824 pixels with a size of 30 m. The Ikonos image consists of a square
27 subset with 2046 x 2046 pixels and 4 m resolution.

28



2.2 Multifractal image analysis

A multifractal analysis is basically the measurement of a statistic distribution and therefore gives useful information even if the underlying structure does not show a full self similar behaviour (Plotnick et al., 1996).

5

A monofractal object can be measured by counting the number N of δ size boxes needed to cover the object. The measure depends on the box size as

$$N(\delta) \propto \delta^{-D_0} \quad (1)$$

where

$$D_0 = \lim_{\delta \rightarrow 0} \frac{\log N(\delta)}{\log \frac{1}{\delta}} \quad (2)$$

is the fractal dimension. D_0 is calculated from slope of a log-log plot.

12

There are several methods for implementing multifractal analysis; in this section the choose moment method (Halsey et al., 1986) is explained. This method uses mainly three functions: $\tau(q)$, known as the mass exponent function, α , the coarse Hölder exponent, and $f(\alpha)$, multifractal spectrum. A measure (or field), defined in two-dimensional image embedding space ($n \times n$ pixels) and with values based on grey tones (for 8 bit goes from 0 to 255), cannot be consider as a geometrical set and therefore cannot be characterized by a single fractal dimension.

20

Applying disjoint covering by boxes in an “up-scaling” partitioning process we obtain the partition function $\chi(q, \delta)$ (Feder, 1989) defined as:

$$\chi(q, \delta) = \sum_{i=1}^{N(\delta)} \mu_i^q(\delta) = \sum_{i=1}^{N(\delta)} m_i^q \quad (3)$$

24



1 where m is the mass of the measure, q is the mass exponent, δ is the length size of the box
 2 and $N(\delta)$ is the number of boxes in which $m_i > 0$. Based on this, the mass exponent function
 3 $\tau(q)$ shows how the moments of the measure scales with the box size:

$$4 \quad \tau(q) = \lim_{\delta \rightarrow 0} \frac{\log \langle \chi(q, \delta) \rangle}{\log(\delta)} = \lim_{\delta \rightarrow 0} \frac{\log \langle \sum_{i=1}^{N(\delta)} m_i^q \rangle}{\log(\delta)} \quad (4)$$

5 where $\langle \rangle$ represents statistical moment of the measure $\mu_i(\delta)$ defined on a group of non
 6 overlapping boxes of the same size partitioning the area studied.

7

8 The singularity index, α , can be determined by the Legendre transformation of the $\tau(q)$ curve
 9 (Halsey, 1986) as:

$$10 \quad \alpha(q) = \frac{d\tau(q)}{dq} \quad (5)$$

11

12 The number of cells of size δ with the same α , $N_\alpha(\delta)$, is related to the cell size as
 13 $N_\alpha(\delta) \propto \delta^{-f(\alpha)}$, where $f(\alpha)$ is a scaling exponent of the cells with common α . Parameter
 14 $f(\alpha)$ can be calculated as:

$$15 \quad f(\alpha) = q\alpha(q) - \tau(q) \quad (6)$$

16

17 Multifractal spectrum (MFS) shown as plot of α vs. $f(\alpha)$, quantitatively characterizes
 18 variability of the measure studied with asymmetry to the right and left indicating domination
 19 of small and large values respectively (Evertsz and Mandelbrot, 1992). The width of the MF
 20 spectrum (Δ) indicates overall variability (Tarquis et al., 2001; 2014).

21



1 3 Results and Discussion

2 3.1 Radiometric influence in the Multifractal spectrum

3 We first discuss the results obtained for the 2046 x 2046 pixels Ikonos image shown in Fig. 1,
 4 in bands combination of false colour (IK#4, IK#3, IK#2 bands combination in RGB
 5 visualization). In Fig. 2 IK#1, IK#2, IK#3, IK#4 bands histograms are shown. In the left
 6 column are histograms with the original radiometric resolution and in the left column the
 7 corresponding histograms rescaled to 8 bits. The histograms present a bimodal structure with
 8 a narrow peak of low value pixels (dark grey) showing a sharp maximum and a wider peak
 9 around a second lower maximum. For bands IK#1, IK#2, IK#3 the narrow peak maximum
 10 corresponds to vegetation, mainly irrigate crops, showing strong water absorption. This effect
 11 is particularly important in band IK#3. High value pixels (lighter grey) correspond to ground
 12 zones with lower vegetation content. However, as vegetation shows high reflectivity in the
 13 near infrared, IK#4 band histogram shows a predominance of high values pixels (lighter grey
 14 pixels) corresponding to dense vegetation parts.

15
 16 We cover the image with boxes of size $\delta = 2^{-n}$ and we change the box size from 2048 to 2
 17 pixels, that is, $\delta = 2048 / 2^n$ with $n = 0, 1, 2, \dots, 10$. For each value of the parameter q , from -5
 18 to +5 with increments of 0.5, the partition function (equation 3) is computed and $\chi(q, \delta)$ vs
 19 $\log \delta$ is plotted in Fig. 3. Each graph contains 11 points. Linear fits of these points with least-
 20 square provides the values of $\tau(q)$ and using Eq. [5-6] $\alpha(q)$ and $f(\alpha)$ are obtained. The MF
 21 spectra $f(\alpha)$ corresponding to the four bands of multispectral Ikonos images are shown in
 22 Fig. 4. Some characteristic parameters obtained from these MF spectra are shown in Table 1.
 23 For each band $\alpha(q)$ values for $q = \{0, 1, 2\}$ are show. The first value corresponds to the
 24 maximum of MFS and it is related to the box-counting dimension where the measure is
 25 defined; the second value is related to information dimension and the third with the
 26 correlation dimension. We split the MF spectra in two sections. Section I correspond to values
 27 $\alpha(q) < \alpha(0)$ or $q > 0$ and section II to values with $\alpha(q) > \alpha(0)$ or $q < 0$. In section I the
 28 amplitude, or semi-width, was calculated with differences $\Delta^+ = \alpha(0) - \alpha(+5)$, and in section II
 29 with $\Delta^- = \alpha(-5) - \alpha(0)$. These two values for Ikonos bands are shown in the two last



1 columns in Table 1. Note that amplitude Δ^+ decreases as bands wavelength grows whereas the
 2 other amplitude Δ^- diminishes.

3

4 To study the influence of radiometric resolution on Ikonos image information complexity, the
 5 original pixel code (11 bits) has been transform to 8 bits through a rescaling based on
 6 minimum and maximum values between 0 and 255, preserving the initial histogram shape. In
 7 figure 2 both the original histograms (left column) and the rescale histograms (right column)
 8 are shown.

9

10 The MF spectrum obtained after this transformation is shown in figure 4 (upper part) and the
 11 corresponding new parameters in Table 2. In this case both Δ^+ and Δ^- increase as the
 12 wavelength increases for the three visible bands, but decreasing for the near infrared band.

13

14 3.2 Spatial resolution influence in the Multifractal spectrum

15 In order to avoid any other effect beside the spatial resolution a comparison between Landsat
 16 (with an original pixel code of 8 bits) and the rescaled histograms from Ikonos is made. In this
 17 section we discuss the results obtained in the MF analysis on 772 x 828 pixels Landsat image
 18 shown in Figure 5, in bands combination of false colour (ETM+#4, ETM+#3 and ETM+#2
 19 bands combination in RGB visualization). The yellow rectangle corresponds to the area
 20 covered for the Ikonos image. Frequency values histograms of these bands are showed in the
 21 right column of Figure 5.

22

23 In the calculations, box sizes range from 512 to 2 pixel, that is, $\delta = 512 / 2^n$ with $n = 0, 1, \dots, 8$.
 24 For each value of the parameters q , from -5 to +5 with increments of 0.5, we compute the
 25 partition function, and $\chi(q, \delta)$ vs $\log \delta$ are plotted in Figure 6. In this case each linear fits
 26 contains only 9 points. The MF spectra, $f(\alpha)$, corresponding to the first four bands of
 27 multispectral Landsat images are shown in Figure 7.

28



1 From a comparison of figures 4 and 7 we see that Landsat images MF spectra are always
2 located inside the corresponding Ikonos MF spectra. For a given value of Hölder exponent α
3 the relation $f_{Landsat}(\alpha) \leq f_{Ikonos}(\alpha)$ is always satisfied. This result means that Landsat images
4 show lower complexity than Ikonos images. As stated in section 3.1 Ikonos satellite data are
5 coded in 11 bits in contrast with Landsat 8 bits coded data. Higher radiometric resolution
6 gives a higher range of possible grey values per pixel. Note that this radiometric resolution
7 effect is manifested in both sections of the MF spectra (I, $q > 0$, and II, $q < 0$).

8

9 The MF spectra parameters are shown in Table 3. In general, Landsat bands present a low
10 degree of multifractality similar to Ikonos images coded at 8 bits. This is also true among the
11 different bands, presenting low variations among them in a range of 1.3 and 1.4. Landsat
12 bands do not show a clear relationship between multifractality and wave length, being the
13 near infrared the lowest multifractality value.

14

15 **4 Conclusions**

16 In this work, we have used MF spectra as a successful technique for analyzing common
17 information contained in multi-spectral images of the site of the Earth surface acquired by two
18 satellites, Landsat-7 and Ikonos, in four common bands in the visible (blue, green and red)
19 and near-infrared wavelength regions used in several vegetation indexes.

20

21 The radiometric resolution has been studied comparing MF spectra of the images acquired by
22 Ikonos-2 coded in 11 bits and transformed in 8 bits code. The results obtained after the
23 histogram transformation in the blue and green bands were the ones you would expected after
24 the simplification applied from 11 to 8 bits, i.e. higher frequency in all the histogram bin
25 values (see figure 2). In contrast, red and infrared bands showed no sensitivity at all to this
26 transformation keeping the same MF spectra. To our knowledge, this is the first time these
27 differences among bands are reported.

28



1 In order to analyse the effect of spatial resolution in each band at 4 m (Ikonos with 8 bits)
2 pixel size and 30 m (Landsat with 8 bits) pixel size are compared. Obviously, the higher the
3 spatial resolution, the higher the Hölder spectrum amplitude in the green and blue bands are.
4 In fact, observing the graphics of the three cases studied (Ikonos 11 bits, Ikonos 8 bits and
5 Landsat 8 bits) both bands gradually reduce their $\alpha(q)$ amplitude in the negative as well as in
6 the positive q values. However, this is not the case for red and infrared bands that present a
7 huge difference between Ikonos and Landsat curves of the MF spectra. This implies that the
8 estimation in the vegetation indices from both sensors will be different.

9
10 In the $q > 0$ region for blue and green bands the sensitivity to both factors are very similar,
11 being the blue band ratio slightly higher. In the other two bands, red and infrared, for the same
12 region only present sensitivity to spatial resolution, showing a similar rate than blue and green
13 bands. Observing the $q < 0$ region for blue and green the behaviour is similar to the positive
14 one but with a lower ratio (between 1 and 2) and once more, the red and infrared bands don't
15 show any sensitivity to radiometric resolution. Nevertheless in the spatial resolution the red
16 band has a ratio similar to blue and green, and infrared shows the highest ratio (around 8)
17 pointing the extreme influence of the lowest values contained, see histograms in figure 2
18 (Ikonos-2 8 and 11 bits) and figure 5 (Landsat-7).

19

20 Acknowledgements

21 Thanks are due to the anonymous referees and the editor for their interest and patient in this
22 work. Discussion and comments suggested by Prof. Jose Manuel Redondo are highly
23 appreciated. This work has been supported by the Ministerio de Economía y Competitividad
24 (MINECO) under Contract Nos. MTM2012-39101 and MTM2015-63914-P.

25

26



1 **References**

- 2 Beaulieu, A. and Gaonac'h, H.: Scaling of differentially eroded surfaces in the drainage
 3 network of the Ethiopian plateau, *Rem. Sens. Environ.*, 82, 111–122, 2002.
- 4 Ben-Ze'ev, E., Karnieli, A., Agam, N., Kaufman, Y., Holben, B., Assessing Vegetation
 5 Condition In The Presence Of Biomass Burning Smoke By Applying The Aerosol-Free
 6 Vegetation Index (AFRI) On MODIS Images, *International journal of remote sensing*, 27,
 7 3203-3221, 2006.
- 8 Cheng, Q. and Agterberg, F.P.: Multifractal modelling and spatial statistics. *Mathematical*
 9 *Geology*, 28(1), 1-16, 1996.
- 10 Cheng, Q.: A new model for quantifying anisotropic scale invariance and for decomposition
 11 of mixing patterns, *Mathematical Geology*, 36, 345–360, 2004.
- 12 De Cola, L., Fractal analysis of a classified Landsat scene. *Photogrammetric Engineering and*
 13 *Remote Sensing* 55(5). 1989.
- 14 Deng, FP, Su, GL, Liu, C, Seasonal Variation Of MODIS Vegetation Indexes And Their
 15 Statistical Relationship With Climate Over The Subtropic Evergreen Forest In Zhejiang,
 16 China, *IEEE GEOSCIENCE AND REMOTE SENSING LETTERS*, 4, 236-240, 2007.
- 17 Dial, G., Bowen, H., Gerlach, F., Grodecki, J. and Oleszczuk, R., IKONOS satellite, imagery
 18 and products. *Remote Sensing of Environment* 88, 23-36. 2003.
- 19 Du, G. and T.S. Yeo. A novel multifractal estimation method and its application to remote
 20 image segmentation. *IEEE Transactions on Geoscience and Remote Sensing* 40(4), 980-982.
 21 2002.
- 22 Evertsz, C.J.G., Mandelbrot, B.B.. In *Chaos and Fractals: New Frontiers of Science*, Peitgen,
 23 H., Jurgens, H. and Saupe Springer-Verlag D., Eds., New York, 921. 1992.
- 24 Feder, J. *Fractals*. Plenum Press, New York, 283pp., 1988.
- 25 Fioravanti, S., *Multifractals: theory and application to image texture recognition*. In “Fractals
 26 in Geosciences and Remote Sensing”, Proceedings of a joint JRC/EARSel Expert meeting.
 27 Ispra. Italy, 14 – 15 April 1994.
- 28 Gaonac'h, H., Lovejoy, S., and Schertzer, D.: Resolution dependence of infrared imagery of
 29 active thermal features at Kilauea volcano. *Int. J. Rem.Sens.*, 24, 2323-2324, 2003.



- 1 Halsey, T.C., Jensen, M.H., Kadanoff, L.P., Procaccia, I. and Shraiman, B.I.. Fractal measures
- 2 and their singularities: the characterization of strange sets. *Phys. Rev. A* **33**, 1141-1151. 1986.
- 3 Harvey, D.C., Gaonac'h, H., Lovejoy, S. and Schertzer, D. : Multifractal characterization of
- 4 remotely sensed volcanic features: a case study from Kilauea volcano, Hawaii, *Fractals*, 10,
- 5 265-274, 2002.
- 6 Hirata, T. and Imoto, M., *Multifractal analysis of spatial distribution of micro-earthquakes in*
- 7 *the Kanto region*, *Geophys. J. Int.* **107**. 1991.
- 8 Huete, A., Miura, T., Yoshioka, H., Ratana, P. and Broich, M., *Indices of Vegetation Activity*
- 9 in "Biophysical Applications of Satellite Remote Sensing". Jonathan M. Hanes Editor,
- 10 Springer, 2014.
- 11 Kravchenko, A.N., Boast, C.W. and Bullock, D.G., *Multifractal analysis of soil spatial*
- 12 *variability*, *Agron. J.* **91**. 1999.
- 13 Laferrière, A. and Gaonac'h, H.: Multifractal properties of visible reflectance fields from
- 14 basaltic volcanoes, *J.Geophys.Res.*, 104(B3), 5115-5126, 1999.
- 15 Lam, N.S. and De Cola, L., *Fractals in Geography*, Prentice Hall, Englewood Cliffs, New
- 16 Jersey. 1993.
- 17 Lam, N.S., *Description and measurement of Landsat TM images using fractals.*
- 18 *Photogrammetric Engineering and Remote Sensing* **56**(2), 1990.
- 19 Lovejoy, S., Pecknold, S., and Schertzer, D.: Stratified multifractal magnetization and surface
- 20 geomagnetic fields-I. Spectral analysis and modelling, *Geophys. J. Int.*, 145, 112–126, 2001a.
- 21 Lovejoy, S., Schertzer, D, Tessier, Y. and Gaonach, H.: Multifractals and resolution-
- 22 independent remote sensing algorithms: the example of ocean colour. *Int. J. Remote Sensing*,
- 23 22(7), 119-1234, 2001b.
- 24 Maître, H. and Pinciroli, M.: Fractal characterization of a hydrological basin using SAR
- 25 satellite images, *IEEE Trans. Geosci. Rem. Sens.*, 37, 175–181, 1999.
- 26 Mandelbrot, B. B. *The Fractal Geometry of Nature*, Freeman, San Francisco. 1983.
- 27 Mika, A.M., Three decades of Landsat instruments. *Photogrammetric Engineering and*
- 28 *Remote Sensing* **63**, 839-852. 1997.



- 1 Parrinello, T. and R.A. Vaughan. Multifractal Analysis and feature extraction in satellite
- 2 imagery. *Int. J. of Remote Sensing* **23**(9), 1799-1825. 2002.
- 3 Plotnick R.E., Gardner, R.H., Hargrove, W.W., Prestegard, K., Perlmutter, M.. Lacunarity
- 4 analysis: a general technique for the analysis of spatial patterns. *Phys. Rev. E.* 53(5), 5461-
- 5 5468. 1996.
- 6 Qiu, H., Lam, N.S., Quattrochi, D.A. and Gamon, J.A., *Fractal characterization of*
- 7 *hyperspectral imagery*, *Photogrammetric Engineering and Remote Sensing* **65**(1). 1999.
- 8 Sánchez, A., Serna, R., Catalina, F. and Afonso, C.N., *Multifractal patterns formed by laser*
- 9 *irradiation in GeAl thin multilayer films*, *Physical Review B*, **46**(1). 1992.
- 10 Schmitt, F., Schertzer, D., Lovejoy, S., and Marchal, P.: Multifractal analysis of satellite
- 11 images: towards an automatic segmentation. In *Fractals in Engineering* (Arcachon: Jules),
- 12 103-109, 1997.
- 13 Tarquis, A.M., Platonov, A., Matulka, A., Grau, J., Sekula, E., Diez, M. and Redondo J. M.
- 14 Application of multifractal analysis to the study of SAR features and oil spills on the ocean
- 15 surface. *Nonlin. Processes Geophys.*, 21, 439-450, 2014.
- 16 Tarquis, A.M., Giménez, D., Saa, A., Díaz, M.C. and Gascó, J.M., *Scaling and multiscaling*
- 17 *of soil pore systems determined by image analysis*, in “Scaling methods in soil physics”. Ed.
- 18 Y. Pachepsky, D.E. Radcliffe and H. Magdi Selim. CRC Press. 2003.
- 19 Tarquis, A.M., Losada, J.C., Benito, R. and Borondo, F., Multifractal analysis of the Tori
- 20 destruction in a molecular Hamiltonian System. *Phys. Rev. E.* **65**, 0126213(9). 2001.
- 21 Tessier, Y., Lovejoy, S., Schertzer, D., Lavalley’e, D., and Kerman, B.: Universal multifractal
- 22 indices for the ocean surface at far red wavelengths. *Geophysical Research Letters*, 20, 1167-
- 23 1170, 1993.
- 24 Turiel, A., Isern-Fontanet, J., García-Ladona, E. and Font, J., Multifractal Method for the
- 25 Instantaneous Evaluation of the Stream Function in Geophysics Flows. *Phys. Rev. Lett.* **95**,
- 26 104502. 2005.
- 27 Wang, X., Xie, H., Guan, H., and Xiaobing, Z, Different responses of MODIS-derived NDVI
- 28 to root-zone soil moisture in semi-arid and humid regions, *Journal of Hydrology*, 340, 12– 24,
- 29 2007.



1 Table 1. Parameters obtained from the multifractal spectrum from each band of Ikonos-2
 2 image with a pixel size of 4 m and a radiometric resolution of 11 bits. . The amplitudes of α
 3 values are presented as Δ^+ and Δ^- corresponding to $\alpha(0)$ - $\alpha(5)$ and $\alpha(-5)$ - $\alpha(0)$ respectively.

4

IKONOS (11bits)	Band	q	$\alpha(q)$	Δ^+	Δ^-
	IK#1	0	2.096	0.418	0.256
		1	1.938		
		2	1.865		
	IK#2	0	2.111	0.377	0.313
		1	1.936		
		2	1.871		
	IK#3	0	2.120	0.348	0.382
		1	1.937		
		2	1.878		
	IK#4	0	2.067	0.290	0.470
		1	1.959		
		2	1.908		

5

6

7

8



1 Table 2. Parameters obtained from the multifractal spectrum from each band of Ikonos-2
 2 image with a pixel size of 4 m and a radiometric resolution of 8 bits. The amplitudes of α
 3 values are presented as Δ^+ and Δ^- corresponding to $\alpha(0)$ - $\alpha(5)$ and $\alpha(-5)$ - $\alpha(0)$ respectively.
 4

IKONOS (8bits)	Band	q	$\alpha(q)$	Δ^+	Δ^-
	IK#1	0	2.044	0.231	0.192
		1	1.971		
		2	1.930		
	IK#2	0	2.060	0.270	0.287
		1	1.963		
		2	1.914		
	IK#3	0	2.102	0.323	0.614
		1	1.945		
		2	1.887		
	IK#4	0	2.056	0.248	0.512
		1	1.966		
		2	1.923		

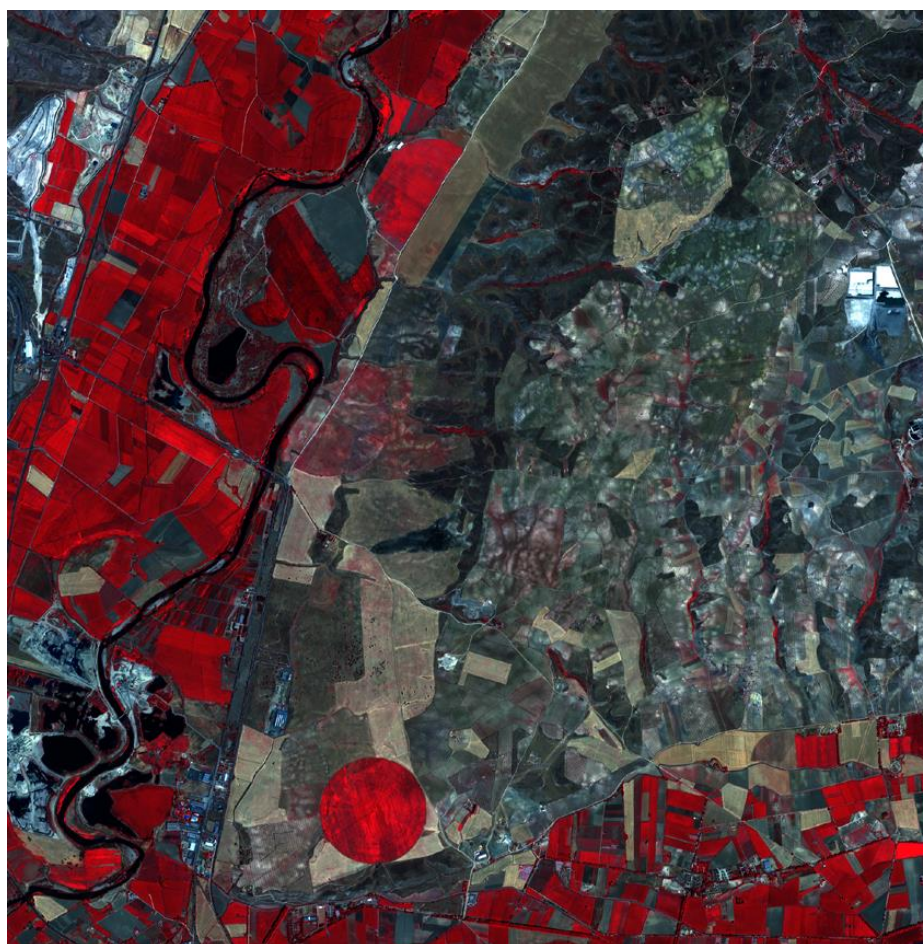
5
 6
 7



1 Table 3. Parameters obtained from the multifractal spectrum from each band of Landsat
 2 image with a pixel size of 4 m and a radiometric resolution of 8 bits. The amplitudes of α
 3 values are presented as Δ^+ and Δ^- corresponding to $\alpha(0)$ - $\alpha(5)$ and $\alpha(-5)$ - $\alpha(0)$ respectively.
 4

Landsat	Band	q	$\alpha(q)$	Δ^+	Δ^-
	ETM+#1	0	2.021	0.160	0.119
		1	1.985		
		2	1.960		
	ETM+#2	0	2.018	0.119	0.119
		1	1.988		
		2	1.970		
	ETM+#3	0	2.016	0.095	0.110
		1	1.989		
		2	1.974		
	ETM+#4	0	2.017	0.106	0.104
		1	1.989		
		2	1.973		

5
 6
 7

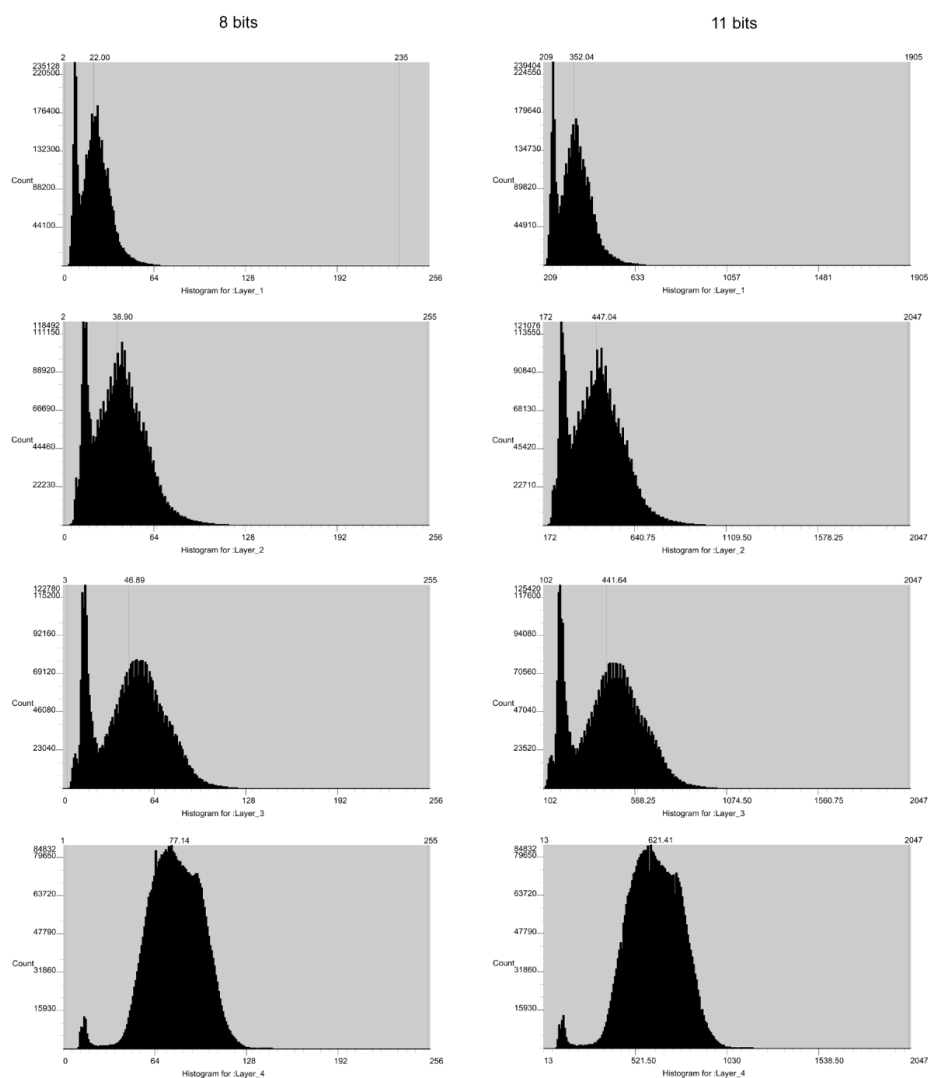


1

2

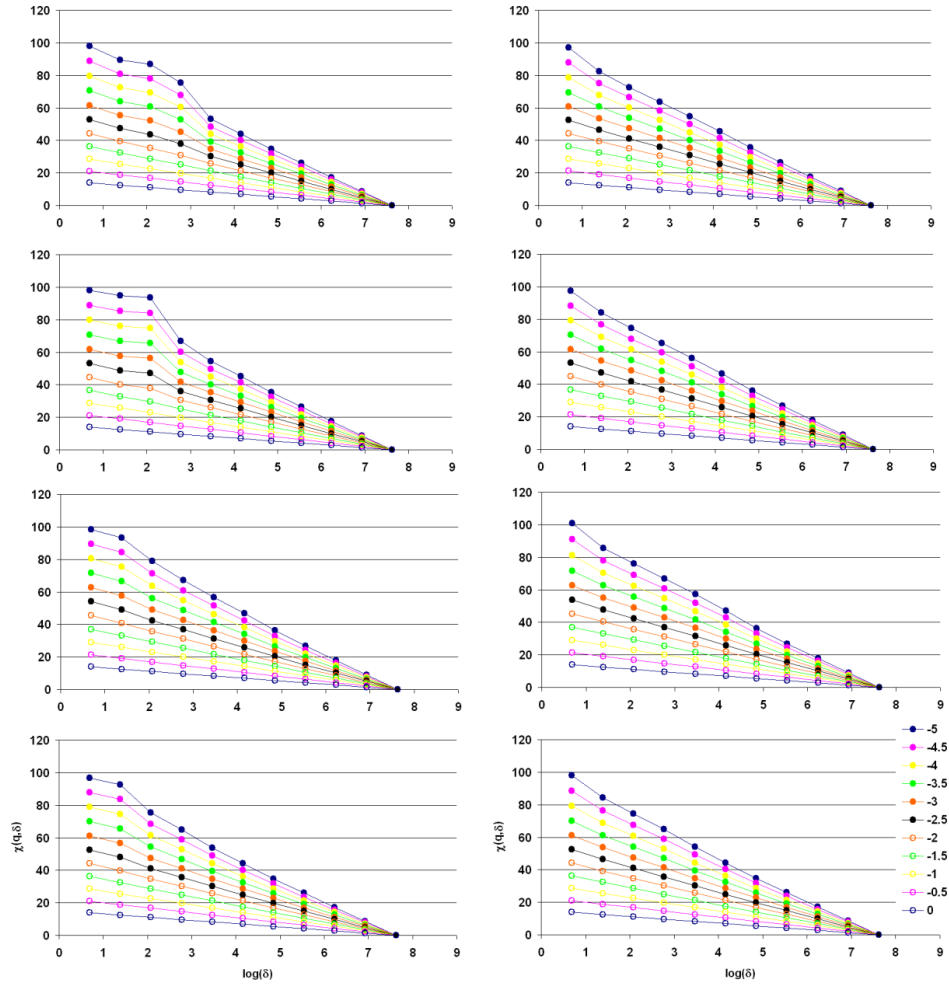
3 Figure 1. The Ikonos-2 image in band combinations of false colour (IK#4, IK#3 and IK#2 in
4 RGB). The image has a size of 2046 x 2046 pixels, each area unit correspond to 4x4 m. The
5 coordinates UTM (zone 30) of the upper left and low right pixel in the image are: ULX =
6 446037 m, ULY = 4441672 m, LRX = 454221 m and LRY = 4433492 m.

7



1
 2 Figure 2. Histograms of the four bands of Ikonos-2 image for the original radiometric
 3 resolution, 11 bits (right), and the minimum-maximum rescale 8 bits radiometric resolution
 4 (left).

5
 6
 7

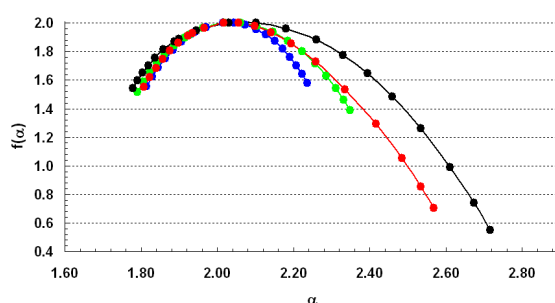


1
 2 Figure 3. Plots of the partition function $\chi(q, \delta)$ versus $\log(\delta)$ for the first four bands of
 3 Ikonos-2 satellite and for $q < 0$ values. From top to bottom we show the results for IK#1,
 4 IK#2, IK#3 and IK#4. All the points are used for the fit and to calculate the slope for different
 5 values of q . The left column correspond to 8-bit image and the right column to 11 bit image.

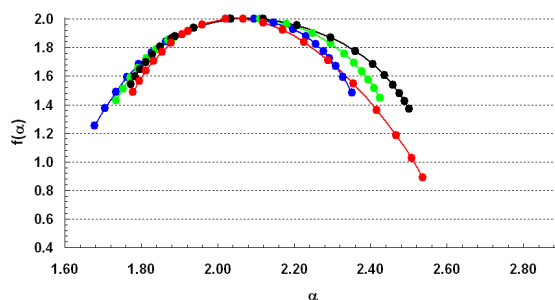
6
 7



Ikonos (8 bits):



Ikonos (11 bits):



1

2

3 Figure 4. Multifractal spectrum of Ikonos-2 images for the original pixel values coded in 11
 4 bits (lower) and the min-max rescale to 8 bits (upper), in each band analyzed: IK#1 in blue
 5 colour, IK#2 in green colour, IK#3 in red colour and IK#4 in black.

6

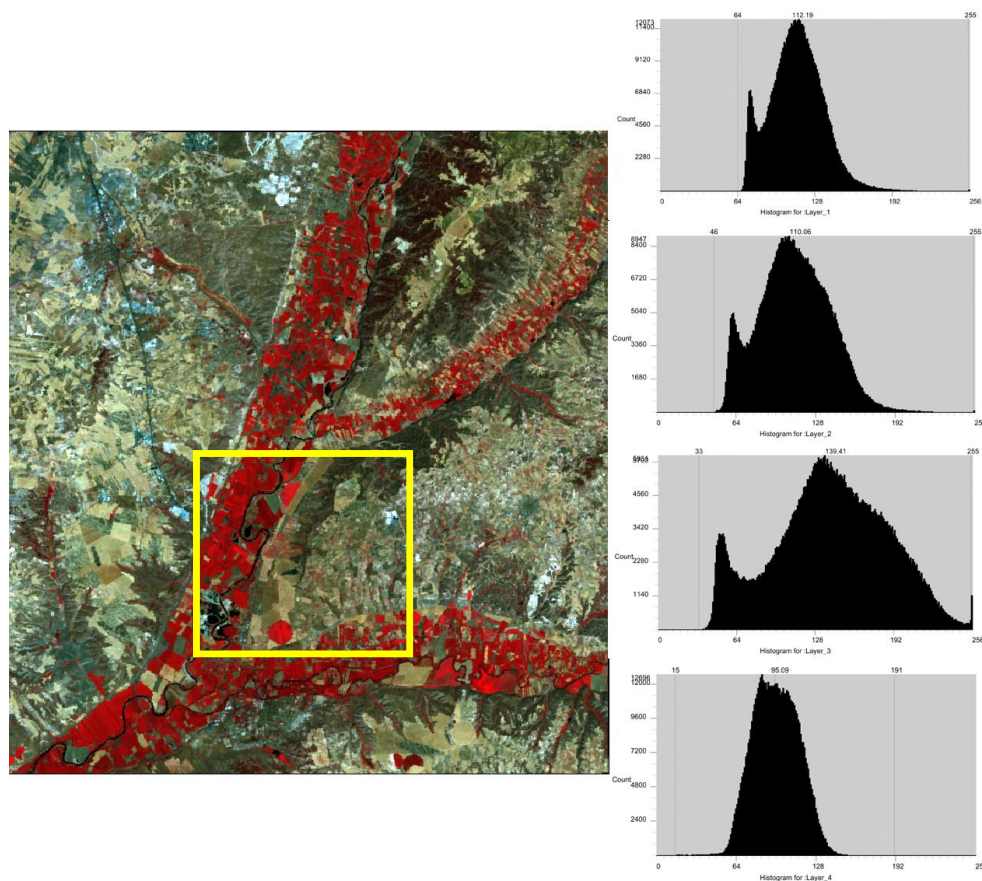
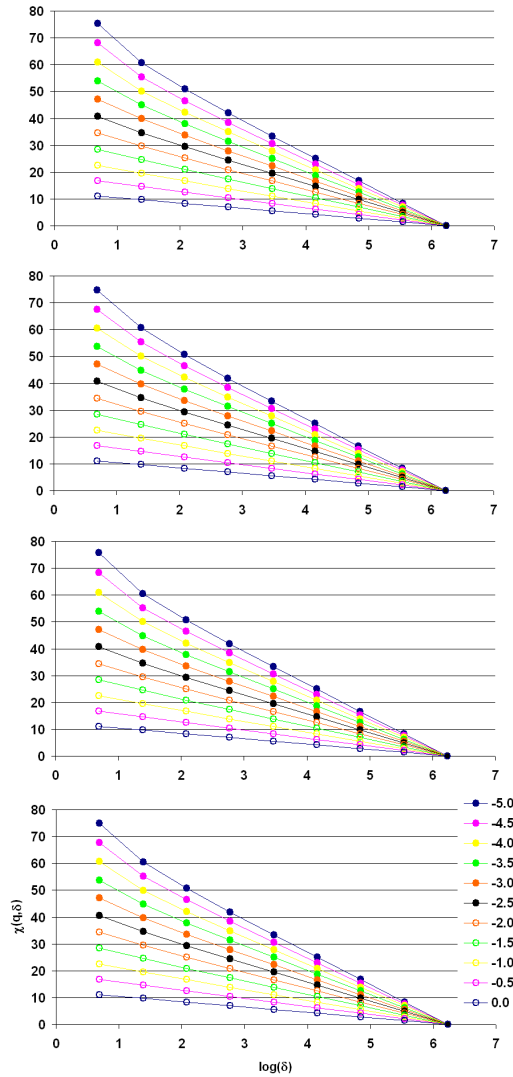
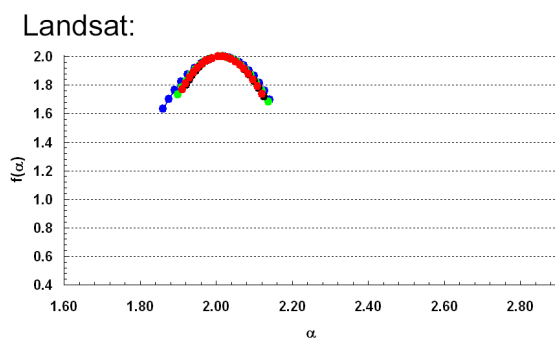


Figure 5. The Landsat-7 image and the histograms for the first four bands: blue (ETM+ #1), green (ETM+ #2), red (ETM+ #3) and near infrared (ETM+ #4). The image has a size of 772x828 pixels, each area unit correspond to 30x30 m. The coordinates UTM (zone 30) of the upper left and low right pixel in the image are: ULX = 438678 m, ULY = 4454134 m, LRX = 461808 m and LRY = 4429324 m.



1
 2 Figure 6. Plots of the partition function $\chi(q, \delta)$ versus $\log(\delta)$ for the first four bands of
 3 Landsat satellite and for $q < 0$ values. From top to bottom we show the results for ETM+#1,
 4 ETM+#2, ETM+#3 and ETM+#4. All the points are used for the regression line and to
 5 calculate the slope for different values of q .

6
 7



1

2

3 Figure 7. Multifractal spectrum of Landsat images for the original pixel values coded in 8
 4 bits, in each band analyzed: ETM+#1 in blue colour, ETM+#2 in green colour, ETM+#3 in
 5 red colour and ETM+#4 in black.